Atomic Spectroscopy

Article

Repeatability-Aware Spectral Fingerprinting and Internal Separability of Nominal Metallic Material Classes by Moderate-Resolution LIBS

Nugzar Gomidze* and David Jakobia

Physics Department, Batumi Shota Rustaveli State University, 35 Ninoshvili Street, Batumi 6010, Georgia

Received: *August 01, 2026;* ***Revised:*** *September 29, 2026;* ***Accepted:*** *September 30, 2026;* ***Available online:*** *September 30, 2026.*

DOI: 10.46770/AS.2026.0072s

ABSTRACT: High spectrum-level classification accuracy in laser-induced breakdown spectroscopy (LIBS) may reflect technical-replicate dependence and acquisition-related confounding rather than generalizable material identification. This study therefore evaluates the within-specimen repeatability and internal spectral separability of nine nominal metallic material classes using a validation-aware analytical workflow. The dataset comprised 181 single-shot spectra obtained from nine physical specimens, with one specimen representing each nominal class. Repeatability descriptors, principal component analysis, Ward hierarchical clustering, and random forest classification were combined with label-permutation testing, acquisition-metadata analysis, and leave-one-acquisition-signature-out assessment. Mean within-class spectral correlations ranged from 0.745 to 0.971, and the first two principal components explained 63.55% of the total variance. random forest out-of-bag resampling completely separated the technical-replicate spectra, whereas weighted accuracy decreased to 93.37% when complete acquisition signatures were excluded. Acquisition metadata predicted material class above chance, and the association between material class and acquisition signature was statistically significant. Label permutation produced a mean null accuracy of 11.18% and an empirical p-value of 0.00498, confirming non-random internal spectral structure. The results demonstrate internal separability among the measured specimens but do not establish identification performance for independently acquired materials. The principal contribution is a transparent validation-aware framework that distinguishes within-dataset separation from external material identification and identifies independent multi-specimen testing under uniform acquisition conditions as the necessary next step.

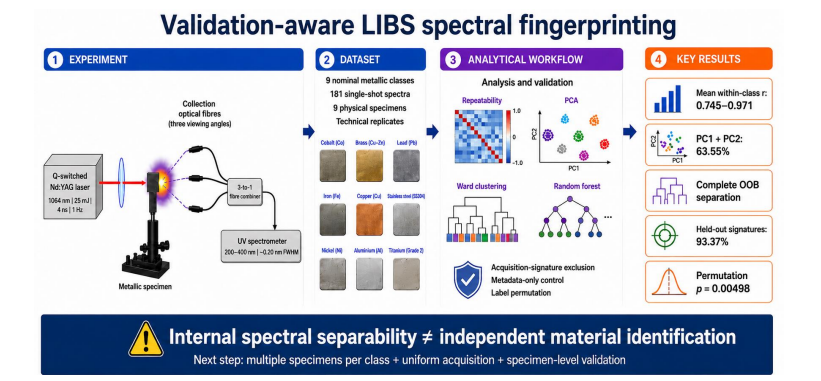

INTRODUCTION

Laser-induced breakdown spectroscopy (LIBS) is a versatile atomic emission technique widely employed for rapid elemental characterization of solids, liquids, and gases. Owing to its minimal sample preparation requirements, real-time response, multi-element detection capability, and applicability in remote or in situ environments, LIBS has become an important analytical tool in materials science, metallurgy, environmental monitoring, planetary exploration, and industrial quality control.[1–5] In metallic materials, the plasma emission spectrum contains characteristic atomic and ionic transitions that provide direct information about elemental composition and material structure.

For known metallic materials, the most direct LIBS identification strategy is to use characteristic atomic or ionic lines, preferably isolated transitions with minimal spectral interference. When wavelength calibration is secure and the optical resolution is sufficient, such line-based discrimination is simpler, more physically interpretable, and may be more transferable than a complex statistical classifier. A spectrometer combining broad spectral coverage with higher optical resolution would therefore

be advantageous for resolving close transitions and selecting interference-free analytical lines. The present study does not claim that full-spectrum machine learning is universally superior to this conventional approach.

The practical difficulty addressed here is different. The archived spectra were recorded with a moderate-resolution instrument (nominal optical resolution approximately 0.20 nm FWHM), for which neighbouring transitions may be unresolved or only partially resolved. Isolated-peak assignments can also be affected by wavelength uncertainty, continuum background, matrix effects, surface condition, and shot-to-shot intensity variation.[1,4–8] Preliminary library-based peak matching consequently produced several ambiguous candidate assignments. Under these conditions, a full-spectrum fingerprint can retain distributed compositional information across multiple spectral regions without requiring every channel to be assigned uniquely to one transition. This approach is complementary to, rather than a replacement for, characteristic-line analysis.

Previous LIBS studies have classified metallic materials using principal component analysis, linear and partial least-squares discriminant analysis, support-vector machines, random forest models, artificial neural networks, and deep-learning architectures. Support-vector machines and random forests have been applied to steel discrimination,[22,23] artificial neural networks to wrought aluminium alloys,[24] and deep-learning models to steel and aluminium-scrap classification.[25,26] These studies demonstrate the feasibility of multivariate classification, while dedicated robustness studies show that reported accuracy depends strongly on experimental design and the unit used for validation.[27,28]

A central interpretive problem is that repeated laser shots from one coupon are technical replicates, not independent material specimens. Random spectrum-level partitioning can therefore place highly related spectra from the same specimen or acquisition session in both training and test sets. Acquisition settings may also become associated with class labels, allowing a model to use integration time, smoothing, averaging, or session-specific structure in addition to composition-related information. Shot-to-shot processing can improve analytical precision,[29,30] but improved agreement among repeated shots does not demonstrate generalization across independently prepared specimens, surface states, instruments, or acquisition sessions.

The unresolved methodological gap is therefore not the absence of another classification algorithm. It is the need to distinguish three questions that are often conflated: whether repeated spectra from a measured specimen are internally consistent, whether the labelled specimens are separable within the available dataset, and whether a model can identify independently acquired materials. This distinction is especially important for low-challenge datasets containing clearly different metals, because a high spectrum-level accuracy can obscure technical-replicate dependence and acquisition-related confounding.

Accordingly, this study evaluates nine nominal metallic material classes using a repeatability- and validation-aware workflow. It asks: 1. how consistent the normalized spectral fingerprints are within each measured specimen; 2. which covariance and material-similarity patterns are revealed by principal component analysis and Ward hierarchical clustering; and 3. to what extent the archived spectra are internally separable by random forest classification when label permutation, acquisition metadata, and leave-one-acquisition-signature-out assessment are considered. Resolution-aware peak detection and NIST Atomic Spectra Database candidate assignments are retained for physical interpretation, but candidate regions are not treated as uniquely resolved high-resolution line identifications.

The contribution is thus a transparent analytical framework and a bounded interpretation, rather than a new classifier or proof of superiority over characteristic-line discrimination. Because one physical specimen represents each nominal class, the principal claim is restricted to within-specimen repeatability and internal spectral separability. External material identification will require uniform acquisition and specimen-level validation using multiple independently prepared specimens, particularly for related pairs such as copper–brass and iron–stainless steel.

EXPERIMENTAL

Experimental procedure and materials. Measurements were performed using a passively Q-switched Nd:YAG laser operating at 1064 nm, with a nominal pulse energy of approximately 25 mJ, a pulse duration of 4 ns, and a repetition rate of 1 Hz. The beam was focused onto the exposed front surface of each specimen using a 100 mm focal-length lens, producing a plasma plume on the irradiated surface. Plasma emission was collected by three optical fibres positioned obliquely relative to the specimen-surface normal, combined through a 3-to-1 fibre combiner, and transmitted through an SMA-905 input to a StellarNet BLUE-Wave UV2 spectrometer. Plasma emission was collected by three optical fibres positioned at viewing angles of 30°, 45°, and 60° relative to the specimen-surface normal. Fig. 1 therefore presents the collection geometry schematically and not to scale. The spectrometer used an f/4 Czerny-Turner configuration, a 2400 grooves mm-1 grating, a 14 μm entrance slit, and a 2048-element CCD array. Spectra were analysed over 200-400 nm with a manufacturer-specified nominal optical resolution of approximately 0.20 nm FWHM. The exported grid had a 0.25 nm sampling interval, yielding 801 channels over the analytical range; this digital interval should not be interpreted as an independent measurement of optical resolution. Wavelength consistency was

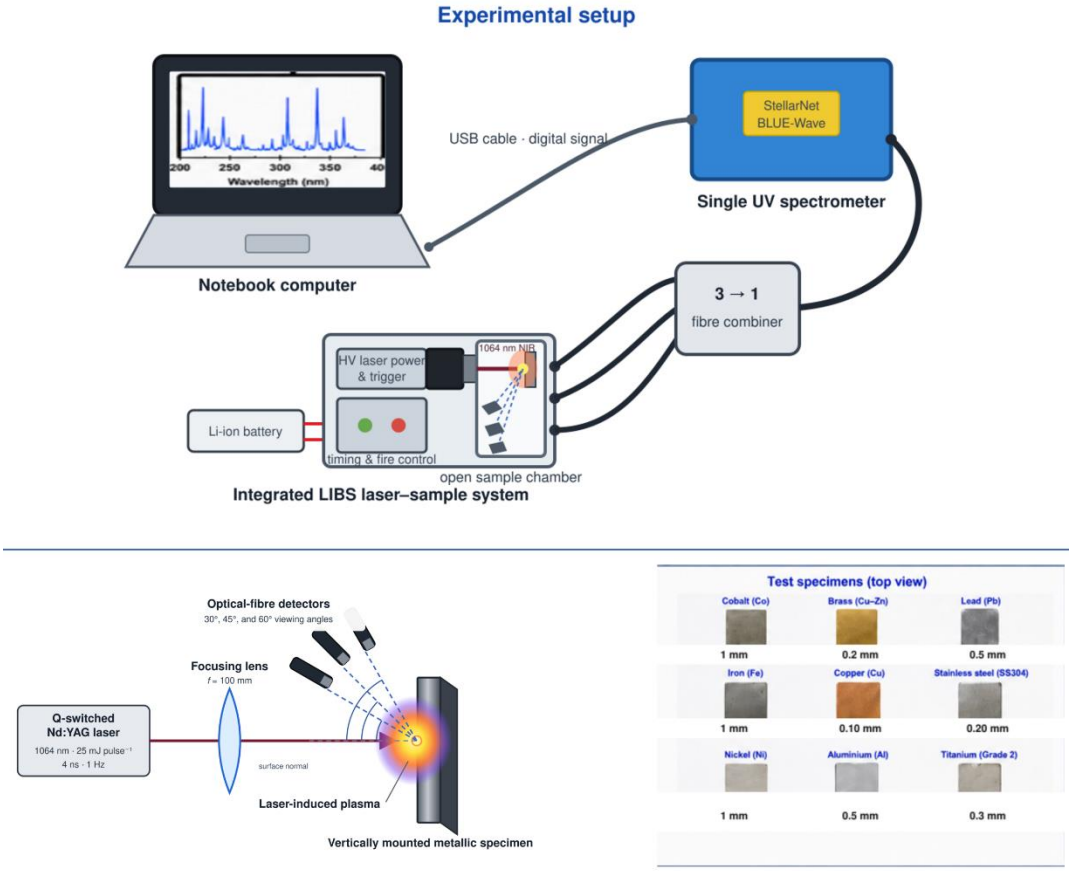

Fig. 1 Schematic of the LIBS experimental arrangement. The focused Nd:YAG laser pulse irradiated the exposed front surface of the vertically mounted metallic specimen at normal incidence, producing a laser-induced plasma on the same surface. Plasma emission was collected by three optical fibres positioned at viewing angles of 30°, 45°, and 60° relative to the specimen surface normal. The fibres were connected through a 3-to-1 fibre combiner to the UV spectrometer, and the recorded signal was transferred to the computer for spectral acquisition and processing. The drawing is schematic and not to scale.

checked internally against prominent NIST ASD regions, including Al I 394.401/396.152 nm, Cu I 324.754/327.396 nm, Zn I 328.233/330.259 nm, and Pb I 368.346 nm. No contemporaneous certified wavelength-calibration spectrum or independent narrow-line FWHM measurement was available.

At the nominal instrumental resolution, closely spaced transitions may appear as unresolved or partially resolved blends. Model-important wavelengths are therefore interpreted as spectral regions rather than uniquely assigned isolated transitions, which limits line-level interpretation and cross-instrument transferability.

Nine nominal material classes were investigated: aluminium, brass, cobalt, copper, iron, lead, nickel, stainless steel, and titanium. One physical specimen represented each nominal class. Supplier-stated grades or purities are summarized in Table 1. Brass was treated as a Cu-Zn alloy and stainless steel as an Fe-based alloy; the remaining specimens were treated according to their nominal elemental-metal designations.

The listed grades and purities were obtained from supplier or product information and were not independently verified by certified chemical analysis. Consequently, the conclusions refer to the measured specimens and their nominal material labels.

Before acquisition, each specimen was wiped with ethanol-wetted cotton and allowed to dry in ambient laboratory air for approximately 1-2 h. Each specimen was mounted on the rotating ceramic support shown in Fig. 1 and analysed in four orientations separated by 90°. Multiple nominal 25 mJ laser pulses were delivered at each orientation, and every acquired spectrum was stored separately (Avg = 1). Surface roughness was not measured, and the archived filenames did not preserve a reliable mapping between individual spectra and the four orientations.

The complete dataset contained 181 single-shot spectra. To assess acquisition heterogeneity, a restricted subset was defined using an integration time of 1000 ms, smoothing disabled, and Avg

Table 1. Specimen information and class-wise composition of the full and restricted LIBS datasets

Nominal class	Supplier-stated grade or purity	Independent specimens	Full dataset, n	1000 ms, Sm off, Avg = 1, n	Remaining spectra, n
Aluminium	1060 aluminium; Al 99.7%	1	23	6	17
Brass	H62 brass; Cu–Zn alloy	1	26	0	26
Cobalt	Co ≥99.99%	1	12	12	0
Copper	Cu ≥99.9%	1	18	4	14
Iron	Fe ≥99.99%	1	11	11	0
Lead	Claimed purity 99.999%	1	14	4	10
Nickel	Ni ≥99.99%	1	12	12	0
Stainless steel	Type 304 stainless steel	1	34	12	22
Titanium	Grade 2 titanium	1	31	15	16
Total	—	9	181	76	105

= 1. This subset contained 76 spectra from eight classes; brass was absent because none of its spectra met these criteria (Table 1).

Spectral Data processing and statistical analysis. The analysis workflow was used for file import, interpolation, normalization, replicate statistics, exploratory multivariate analysis, and random forest classification. The final dataset comprised 181 exported single-shot spectra. Spectra were interpolated to a common 0.25 nm grid over 200–400 nm.

Spectral normalization. A restricted acquisition subset was defined using three metadata criteria: an integration time of exactly 1000 ms, software smoothing disabled, and single-shot acquisition with Avg = 1. The subset contained 76 spectra from eight nominal material classes: aluminium (n = 6), cobalt (n = 12), copper (n = 4), iron (n = 11), lead (n = 4), nickel (n = 12), stainless steel (n = 12), and titanium (n = 15). Brass was absent because none of its 26 spectra satisfied all three criteria. This subset was used to examine raw signal-level variation under more uniform acquisition settings and was not treated as independent-specimen or classifier validation.

For each spectrum i, the fifth percentile of its raw intensity values was used as an empirical baseline:

$$b_i = Q_{0.05}\left(\{I_i(\lambda_k)\}_{k=1}^{N_\lambda}\right), \qquad (1)$$

where $Q_{0.05}$ denotes the fifth percentile and $I_i(\lambda_k)$ is the raw detector intensity of spectrum i at wavelength channel λ_k. Baseline-corrected intensities were calculated as:

$$I_i^{\mathrm{bc}}(\lambda_k) = \max[I_i(\lambda_k) - b;\ 0]. \qquad (2)$$

Each baseline-corrected spectrum was then independently scaled to its own maximum:

$$I_i^{\mathrm{norm}}(\lambda_k) = \frac{I_i^{\mathrm{bc}}(\lambda_k)}{\max\limits_{1\le j\le N_\lambda} I_i^{\mathrm{bc}}(\lambda_j)}. \qquad (3)$$

Thus, the maximum corrected intensity of each normalized spectrum was equal to unity. This preprocessing reduced differences in absolute signal amplitude and facilitated comparison of relative spectral shapes. However, independent maximum normalization can also remove physically meaningful variation in total plasma-emission intensity. Accordingly, conclusions based on normalized spectra were restricted to relative spectral fingerprints rather than absolute emission strength.

To retain information about absolute signal variation, the mean raw detector intensity of each stored single-shot spectrum was calculated before baseline correction and normalization Eq. (4):

$$\bar{I}_i = \frac{1}{N_\lambda}\sum_{k=1}^{N_\lambda} I_i(\lambda_k), \qquad N_\lambda = \frac{400.00 - 200.00}{0.25} + 1 = 801. \qquad (4)$$

here, $\bar{I}_i$ represents the mean unprocessed detector count of spectrum i over the 200–400 nm analytical interval and not the intensity of an individual emission line.

For each nominal material class g, the spectrum-level values of $\bar{I}_i$ were summarized using the arithmetic mean, sample standard deviation, median, interquartile range, and coefficient of variation. The class-wise mean and sample standard deviation were calculated as:

$$\mu_g = \frac{1}{n_g}\sum_{i=1}^{n_g} \bar{I}_{gi}, \qquad (5)$$

$$s_g = \sqrt{\frac{1}{n_g - 1}\sum_{i=1}^{n_g}\left(\bar{I}_{gi} - \mu_g\right)^2}. \qquad (6)$$

The coefficient of variation was expressed as a percentage:

$$CV_g = 100\frac{s_g}{\mu_g}. \qquad (7)$$

The interquartile range was defined as:

$$IQR_g = Q_{0.75,g} - Q_{0.25,g}. \qquad (8)$$

These descriptive comparisons were performed for both the

complete dataset of 181 spectra and the restricted 1000 ms, unsmoothed, single-shot subset (Avg = 1). Raw mean intensity was interpreted as a descriptive measure of the overall detector signal and shot-to-shot variability. Because it may also depend on acquisition settings, focusing, ablation efficiency, plasma evolution, and surface condition, it was not treated as a composition-specific identifier.

Mean spectrum and spectral variability. For each nominal material class, the mean normalized spectrum was calculated using Eq. (9) [12]:

$$\bar{I}(\lambda_k) = \frac{1}{N}\sum_{i=1}^{N} I_i(\lambda_k). \quad (9)$$

For each material, the mean and sample standard deviation were calculated across all replicate spectra at every wavelength channel. Because each spectrum was independently baseline-corrected and maximum-scaled, the standard deviation represents variation in relative spectral shape, not absolute-emission repeatability.

Replicate correlation analysis. Pairwise similarity between normalized replicate spectra a and b was evaluated using the Pearson correlation coefficient defined in Eq. (10) [18]:

$$r_{ab} = \frac{\sum_{k=1}^{N_\lambda}[I_a(\lambda_k) - \bar{I}_a]\,[I_b(\lambda_k) - \bar{I}_b]}{\sqrt{\sum_{k=1}^{N_\lambda}[I_a(\lambda_k) - \bar{I}_a]^2}\sqrt{\sum_{k=1}^{N_\lambda}[I_b(\lambda_k) - \bar{I}_b]^2}}. \quad (10)$$

A correlation coefficient approaching unity indicates highly reproducible spectral measurements.

Spectral entropy. The spectral entropy was employed as a measure of spectral complexity and information content. After converting the normalized spectrum into a probability distribution [19]:

$$p_k = \frac{I(\lambda_k)}{\sum_{j=1}^{N_\lambda} I(\lambda_j)}. \quad (11)$$

The normalized spectral intensities were converted into a probability distribution using Eq. (11) the normalized Shannon entropy was calculated as Eq. (12):

$$H = -\frac{\sum_{k=1}^{N_\lambda} p_k \ln p_k}{\ln N_\lambda}. \quad (12)$$

where N_λ is the total number of spectral channels. Higher entropy values correspond to more complex spectra with a broader distribution of spectral information.

Peak detection and peak density. Peaks were detected in the mean normalized spectrum using a minimum prominence of 0.04. The nominal minimum separation was set to 0.30 nm (1.5 times the manufacturer-specified optical FWHM); however, because the exported wavelength grid was sampled at 0.25 nm intervals, the effective discrete peak separation was constrained by the channel grid and was not interpreted as sub-channel spectral resolution. Peak counts are algorithm-dependent descriptors rather than direct counts of all physical atomic transitions. The nominal minimum peak separation was defined according to Eq. (13):

$$\Delta\lambda_{\min} = 1.5\ \mathrm{FWHM}_{\mathrm{inst}} = 1.5(0.20\ \mathrm{nm}) = 0.30\ \mathrm{nm}. \quad (13)$$

For the moderate-resolution UV spectrometer, $FWHM_{inst} = 0.20$ nm ; thus, yielding a minimum peak spacing of approximately 0.30 nm.

Peak density was calculated using Eq. (14):

$$PD = \frac{N_{\mathrm{peaks}}}{\lambda_{\max} - \lambda_{\min}}. \quad (14)$$

where N_{peaks} represents the number of detected peaks.

Spectral stability index. The spectral stability of replicate measurements was quantified using the coefficient of variation Eq. (15) [4]:

$$CV(\lambda_k) = \frac{s(\lambda_k)}{|\bar{I}(\lambda_k)|}. \quad (15)$$

where $s(\lambda_k)$ is replicate spectra of sample standard deviation.

The Spectral Stability Index was calculated from the mean coefficient of variation over the retained wavelength channels using Eq. (16). [1]:

$$SSI = 1 - \frac{1}{|\,\Omega\,|}\sum_{\lambda_k \in \Omega} C\,V(\lambda_k), \qquad \Omega = \{\lambda_k : \bar{I}(\lambda_k) > 0.05\}. \quad (16)$$

For wavelength channels whose mean normalized intensity exceeded 0.05, the coefficient of variation was calculated and averaged; the spectral stability index was SSI = 1 – mean (CV). SSI is an empirical within-dataset descriptor. It should not be interpreted as an instrument-independent physical constant or as a substitute for laser pulse-energy stability.

Principal component analysis (PCA). PCA was calculated on the normalized feature matrix after mean centering each wavelength channel without unit-variance autoscaling. Economy-size singular-value decomposition was used to avoid rank-deficiency warnings when the number of wavelength channels exceeded the number of spectra. This exploratory use of PCA is consistent with our earlier application of dimensionality reduction to fluorescence excitation-emission spectra of Georgian wines [21]. PCA scores and loadings in the present LIBS dataset are interpreted as covariance structure, not as an independently validated classifier. The mean-centred spectral matrix was decomposed according to

Eq. (17):

$$X = TP^T + E. \qquad (17)$$

where T, P, and E denote the score, loading, and residual matrices, respectively.

Similarity and hierarchical clustering. For descriptive material-level comparison, one mean normalized spectrum was calculated per material. Pearson correlations were calculated between these nine means. Euclidean distances between the mean spectra were then clustered with Ward linkage. Because only one class mean entered per material, the dendrogram is descriptive and provides no uncertainty estimate.

Random-forest classification. A random forest comprising 300 classification trees was fitted to the normalized spectra. Predictions were obtained by out-of-bag aggregation, and per-class precision, recall, specificity, F1, balanced accuracy, and Matthews correlation coefficient were calculated. Uncertainty was assessed by 50 repeated 20% holdout partitions. Wavelength importance was calculated as mean decrease in impurity (MDI; Gini importance) across 50 independently seeded 300-tree fits; the between-fit SD, mean rank, and frequency of inclusion among the ten highest-ranked channels were retained. Importance was aggregated into 0.5 nm regions. Targeted copper–brass, iron–stainless-steel, and cobalt–nickel models generated pairwise confusion matrices and wavelength-importance profiles. As a negative control, material labels were randomly permuted 200 times and 150-tree OOB models were fitted; the empirical p-value was calculated as (1 + number of null accuracies at least as large as the observed accuracy)/(200 + 1). Acquisition-signature exclusion and metadata-only five-fold validation were used to assess confounding.

- Overall classification accuracy,
- Confusion matrix,
- Out-of-bag error,
- Wavelength importance ranking.

OOB evaluation separates bootstrap-included and bootstrap-excluded spectra for individual trees, but spectra from the same physical specimen may occur on both sides. The reported value therefore measures internal spectrum-level discrimination and may be optimistic for new specimens, new surface states, or new acquisition sessions.

Because each nominal material class was represented by only one physical specimen, specimen-level train–test separation could not be performed. The OOB and repeated random-holdout procedures can assign technical-replicate spectra from the same specimen to both the training and test partitions. These procedures therefore assess only spectrum-level internal separability within the archived dataset and do not estimate generalization to independently prepared specimens. The leave-one-acquisition-signature-out analysis evaluates sensitivity to acquisition configuration but does not resolve same-specimen dependence and should not be interpreted as independent-specimen validation.

RESULTS AND DISCUSSION

Normalized spectral fingerprints and repeatability. The raw single-shot and normalized mean spectra (Figs. S1–S9) showed strong material-dependent structure over 200–400 nm. The first panel of each figure retains the raw instrument intensity and therefore exposes acquisition-related amplitude variation; the second and third panels use independently normalized spectra to compare relative spectral shapes and correlations.

For direct visual comparison, Fig. 2 presents the normalized class-mean spectra of all nine nominal materials on common wavelength and intensity scales. The panels show distinct peak distributions and spectral-envelope structure, while related materials retain partially shared regions. Because each class is represented by technical replicates from one physical specimen, these curves are within-dataset fingerprints rather than general reference spectra for the material classes.

Figure 3 compares the unnormalized spectrum-level mean detector counts across the nominal material classes. Each point represents one stored single-shot spectrum, the centre line denotes the median, and the box represents the interquartile range. Across all 181 spectra, mean detector counts ranged from 481.8 for nickel to 2458.4 for titanium. Iron showed the lowest relative dispersion (CV = 15.5%), whereas aluminium, brass, titanium, and stainless steel showed the largest relative dispersion (CV = 58.5–63.2%). Titanium had the highest full-dataset mean, but its broad distribution indicates that this signal level was not consistent across individual shots.

Restriction to spectra acquired at 1000 ms without smoothing and with Avg = 1 reduced the comparison to 76 spectra from eight classes; brass was absent because no brass spectrum satisfied these acquisition criteria. The material ordering changed substantially. Titanium decreased from a full-dataset mean of 2458.4 counts to 789.6 counts, lead decreased from 1366.0 to 258.3 counts, whereas iron remained approximately 945 counts. This reordering provides direct evidence that absolute signal amplitude was influenced by acquisition configuration in addition to material- and plasma-dependent response.

The broad copper distribution in the restricted subset should be interpreted cautiously because it contains only four spectra. Possible

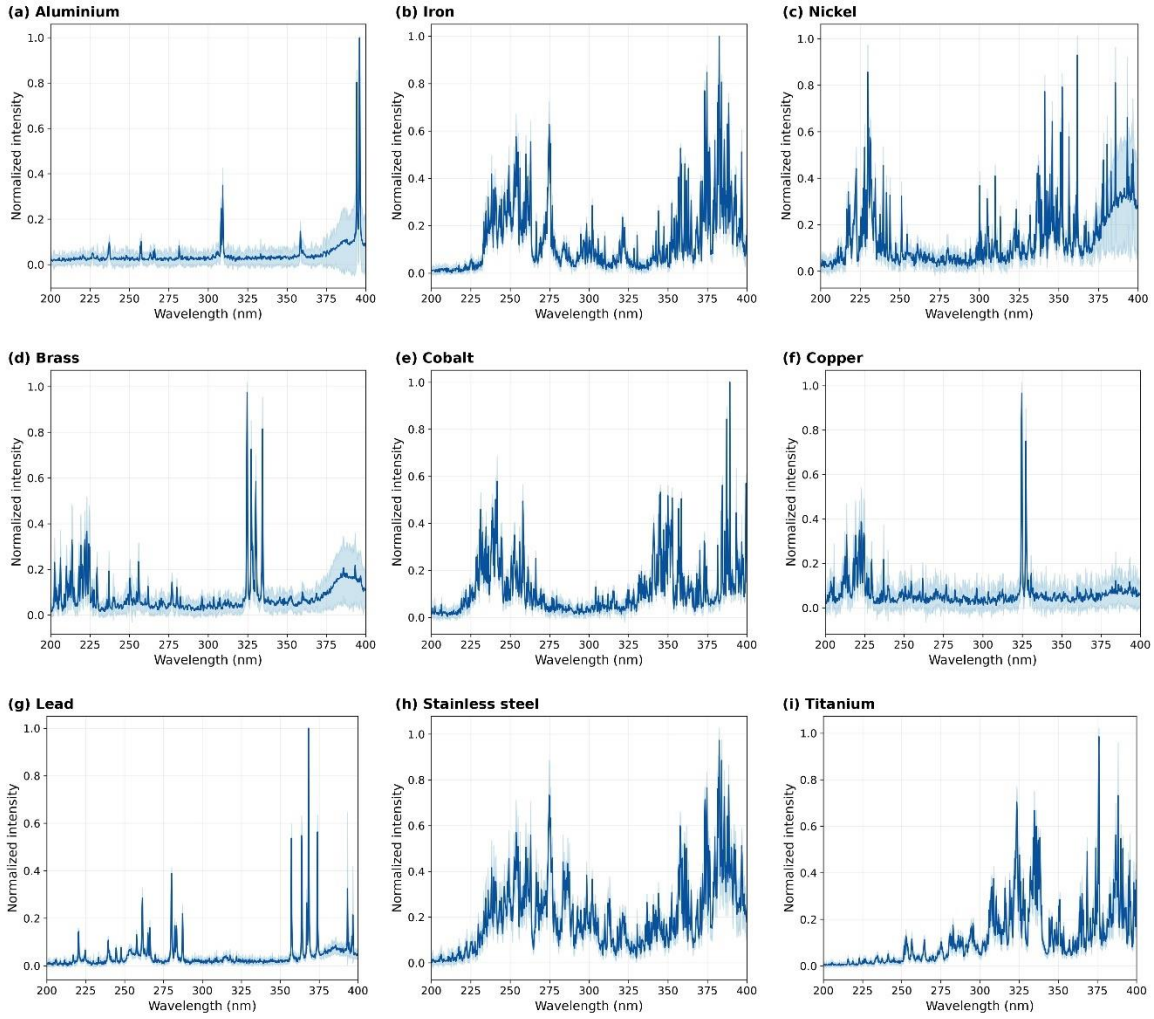

Fig. 2 Normalized class-mean LIBS spectra of the nine nominal materials over 200-400 nm: (a) aluminium, (b) iron, (c) nickel, (d) brass, (e) cobalt, (f) copper, (g) lead, (h) stainless steel, and (i) titanium. Solid curves show the mean of independently normalized technical-replicate spectra, and shaded bands show ±1 SD. The figure illustrates within-dataset spectral differences and should not be interpreted as independent specimen-level validation.

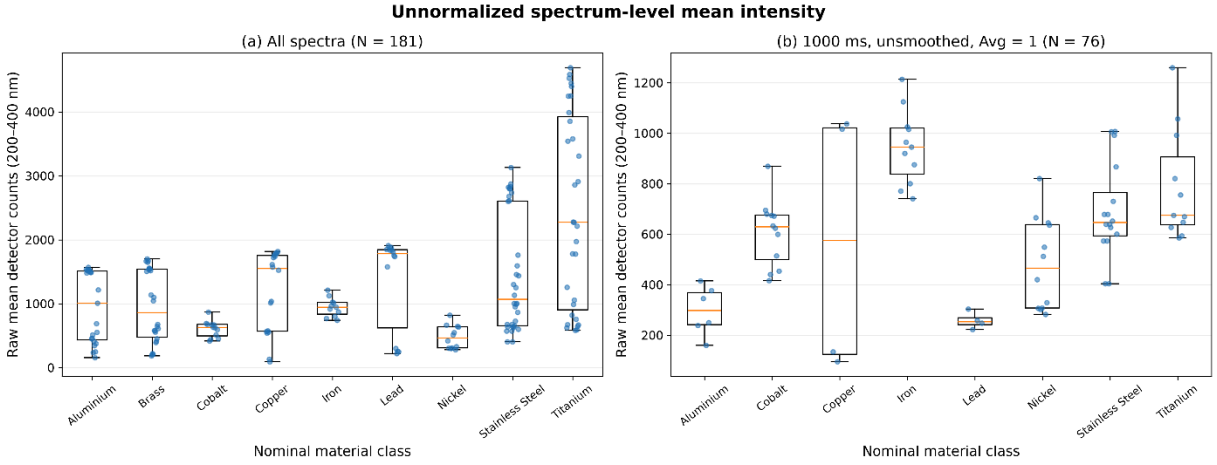

Fig.3 Unnormalized spectrum-level mean detector counts over 200–400 nm by nominal material class: (a) all 181 spectra; and (b) the 1000 ms, unsmoothed, single-shot subset (Avg = 1; N = 76). Points represent individual spectra and boxes summarize their distributions. Brass is absent from panel (b) because no brass spectrum satisfied the restricted acquisition criteria. Absolute amplitude is descriptive and may reflect acquisition conditions, ablation efficiency, plasma emission, focusing, surface state, and matrix effects.

Table 2. Spectral fingerprinting and within-session repeatability metrics

Material	N	Mean pairwise correlation	Normalized entropy	Detected peaks	SSI
Aluminum	23	0.854	0.942	9	0.012
Brass	26	0.810	0.953	42	0.345
Cobalt	12	0.944	0.943	109	0.732
Copper	18	0.787	0.955	44	0.141
Iron	11	0.971	0.934	109	0.793
Lead	14	0.917	0.919	20	0.696
Nickel	12	0.745	0.950	105	0.565
Stainless steel	34	0.892	0.958	121	0.706
Titanium	31	0.941	0.928	82	0.749

contributions include focusing differences, local surface condition, crater evolution, ablated mass, and pulse-to-pulse energy variation; these mechanisms were not measured independently. Consequently, raw mean intensity is used here as a signal-level repeatability diagnostic, whereas material fingerprint comparison and multivariate modelling rely primarily on independently normalized spectral shapes.

Across the 181 spectra, mean within-class correlations ranged from 0.745 for nickel to 0.971 for iron (Table 2). Cobalt (0.944), titanium (0.941), lead (0.917), and stainless steel (0.892) showed comparatively high correlation, whereas copper (0.787), brass (0.810), and aluminium (0.854) were more variable. Minimum correlations remained low for aluminium (0.414) and copper (0.406).

Accordingly, the stability metrics are reported as empirical properties of this dataset. They do not establish material-intrinsic repeatability because laser pulse-energy RSD and specimen roughness were not recorded, and the inspected file headers demonstrate that integration time and instrument-software smoothing were not uniform across all archived spectra.

Spectral information descriptors. Resolution-constrained peak counts ranged from 9 for aluminium to 121 for stainless steel; cobalt and iron each yielded 109 detected peaks under the same rule. These values summarize detected structure under a fixed prominence and separation rule; they are not direct counts of resolved atomic transitions and cannot by themselves establish greater analytical information content.

Normalized spectral entropy varied over a comparatively narrow range. Because entropy, peak count, and SSI respond differently to normalization, background, spectral congestion, and replicate variation, they are reported separately. No claim is made that a single composite index provides a universal measure of LIBS spectral quality.

Relationship between repeatability and material response. Copper combined a comparatively large number of detected peaks with low replicate correlation and low SSI, whereas iron combined a rich spectrum with high correlation and SSI. This contrast shows that spectral richness and repeatability are distinct. Possible causes include differences in reflectance at 1064 nm, thermal conductivity, melting and ablation thresholds, crater evolution, and local alloy heterogeneity.[4,20] These mechanisms were not measured independently and are therefore presented as hypotheses rather than causal conclusions.

Principal component analysis. PCA was used to inspect covariance structure after per-spectrum normalization and wavelength-channel mean centring without autoscaling. PC1 explained 46.33% and PC2 explained 17.22%, giving 63.55% cumulative variance (Fig. 4). The first five and ten components explained 84.27% and 93.33%, respectively.

The score plot showed separated regions for several materials, including titanium and stainless steel. Given the conspicuous compositional differences among most classes, this separation is expected and should not be treated as evidence of a difficult classification task.

The first ten components accounted for 93.33% cumulative variance. PC3 explained a further 8.42%; therefore, PC1–PC3 and PC2–PC3 projections were also inspected to ensure that structure hidden from the PC1–PC2 plane was not ignored. PCA loadings were compared at the region level with repeated Random Forest importance and candidate NIST transitions; isolated loadings were not treated as elemental confirmation.

Hierarchical clustering. Hierarchical clustering results are presented in Fig. 4d. Ward clustering of the nine mean spectra placed brass and copper close together, consistent with their shared Cu-dominated features. Iron and stainless steel were also related, consistent with the Fe contribution to stainless steel. These relationships are chemically plausible, but the dendrogram is exploratory because it contains one mean spectrum per class and no resampling-based uncertainty.

The clustering is therefore used to summarize spectral similarity, not to argue that hierarchical methods are required to distinguish obviously different bulk materials.

Random forest internal-separability analysis. The 300-tree random forest produced a diagonal OOB confusion matrix for the 181 spectra, corresponding to 100% spectrum-level internal accuracy. All per-class OOB metrics were therefore 1.00. However, this resampling scheme still allows spectra from the same physical specimen and acquisition setting on both sides of evaluation.

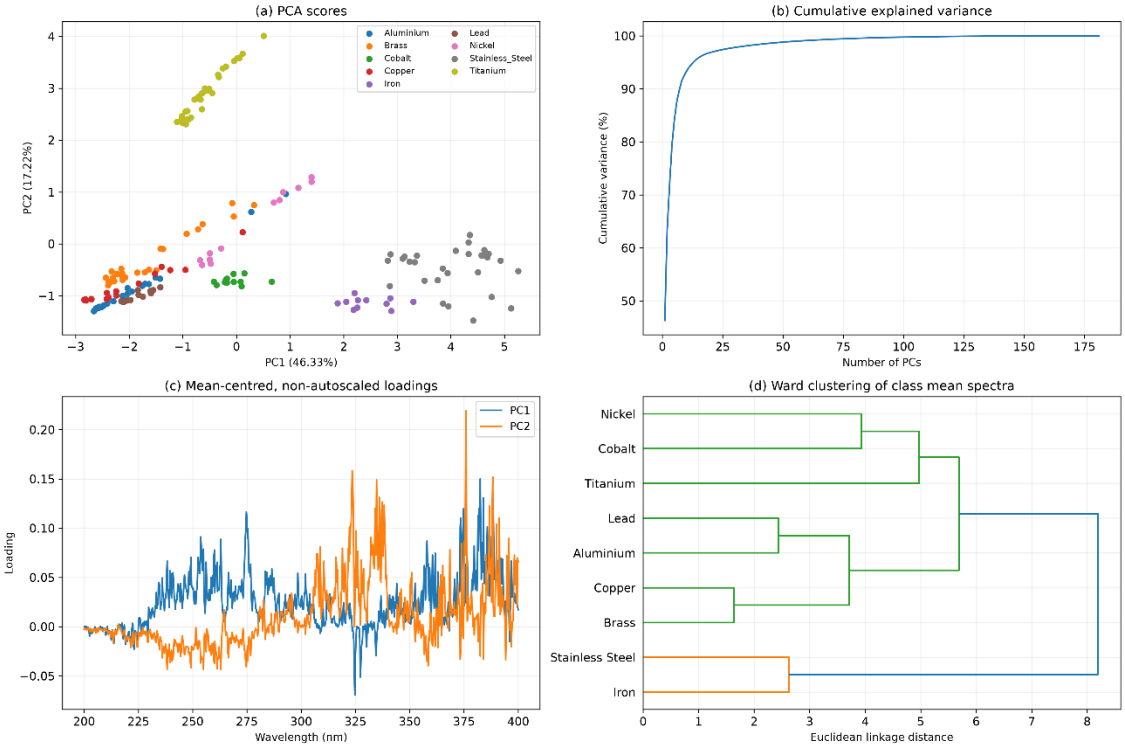

Fig. 4 Multivariate overview of the 181 normalized LIBS spectra: (a) PC1–PC2 scores; (b) cumulative explained variance; (c) mean-centred, non-autoscaled PC1/PC2 loadings; and (d) Ward clustering of the nine class mean spectra. PCA and clustering are exploratory and are not independent validation procedures.

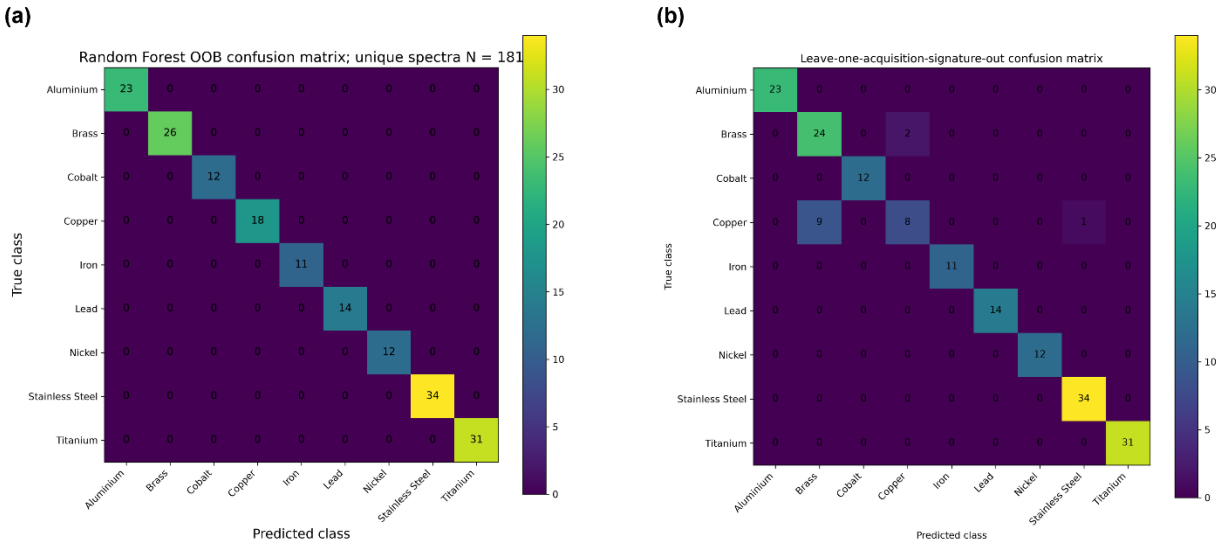

Fig. 5 Comparison of Random-forest classification performance: (a) spectrum-level out-of-bag confusion matrix for 181 spectra, showing complete internal separability; and (b) aggregated confusion matrix from leave-one-acquisition-signature-out validation, in which complete integration-time/smoothing/trigger signatures were excluded in turn (weighted accuracy 93.37%).

This result demonstrates complete internal separation of the technical-replicate spectra but cannot be interpreted as an unbiased estimate of classification performance for unseen physical specimens.

Repeated spectrum-level holdout tests also separated copper–brass, iron–stainless-steel, and cobalt–nickel pairs within this archive (mean overall holdout accuracy 99.95% ± 0.38 percentage points across 50 partitions). This result remains subject to same-specimen leakage and is not treated as external validation. The

leading model-important regions were compared with NIST reference transitions and the measured class-wise mean responses (Table S1). The most interpretable candidates include Al-associated regions at 394.0–394.5 and 396.0–396.5 nm, Cu-associated regions at 324.5–325.0 and 327.0–327.5 nm, Zn-sensitive brass regions at 328.0–328.5 and 330.0–330.5 nm, and Pb-sensitive regions at 280.0–280.5 and 368.0–368.5 nm.

The repeated random-holdout result is reported as an internal resampling assessment rather than an independent validation result because technical replicates from the same physical specimen could occur in both partitions.

A stricter leave-one-acquisition-signature-out analysis held out each of eight integration-time/smoothing/trigger signatures in turn and correctly classified 169 of 181 spectra (weighted accuracy 93.37%; Fig. 5(b)). Signature-specific accuracies ranged from 76.67% to 100%. Acquisition metadata alone achieved 37.61% ± 6.08 percentage points balanced accuracy in repeated five-fold validation, compared with a nine-class chance level of 11.11%. The significant material–signature association (Cramér's V = 0.556, $p = 6.2 \times 10^{-52}$) confirms acquisition confounding and supports treating 100% OOB accuracy only as internal separability.

The correspondence between model importance, PCA loadings, candidate transitions, and class-associated mean-spectrum enhancement provides a plausible physical link between nominal composition, spectral fingerprint, and classification. The regions containing Al I 394.401/396.152 nm are enhanced in aluminium; Cu I 324.754/327.396 nm is enhanced in copper-bearing spectra; Zn I 328.233/330.259 nm is consistent with additional brass response; and Pb I 368.346 nm is enhanced in lead. The 334.5–335.0 and 357.0–357.5 nm intervals remain blended candidates. Repeated-fit rank stability and top-ten frequency are reported to prevent interpretation of seed-dependent regions.

The visibly distinct class-mean spectra in Fig. 2 confirm that several of the nominal materials could also be discriminated using selected characteristic lines. The multivariate workflow was not introduced because such clearly different metals necessarily require machine learning, nor was it intended to outperform an optimized line-based classifier. Its purpose was to quantify repeatability, distributed full-spectrum separability, acquisition-related confounding, and validation dependence within the archived moderate-resolution dataset. A direct comparison with a line-selected classifier using independently acquired specimens remains an appropriate subject for future work.

Scope, limitations, and implications. The workflow demonstrates complete spectrum-level internal separation of 181 spectra and 93.37% weighted accuracy when entire acquisition signatures are excluded. The latter is the more conservative classification result. Position-grouped results remain unavailable because no reliable file-to-orientation map was retained.

The principal limitation of the classification analysis is the absence of independently prepared specimens within each nominal material class. Because all replicate spectra for a given class originated from one physical specimen, the model may partly distinguish specimen-specific properties, including surface condition, oxide state, local heterogeneity, crater evolution, or acquisition-session characteristics. Neither OOB resampling nor random spectrum-level holdout can separate these effects from general material-class information. The acquisition-signature exclusion analysis provides a more conservative assessment of sensitivity to instrumental configuration, but it does not constitute specimen-level validation. Consequently, the reported performance metrics are restricted to internal separability of the measured specimens, and no claim is made regarding identification accuracy for unseen coupons, independent batches, or different alloy grades.

The principal limitations are missing pulse-energy stability measurements, heterogeneous acquisition configurations, unavailable position labels, unequal class sizes, supplier-stated rather than independently verified composition for several specimens, unmeasured oxide thickness and surface roughness, possible self-absorption, detector-response variation in the UV range, and moderate spectral resolution relative to dense atomic-line fields. The cobalt, iron, and nickel entries should be interpreted as supplier-reported high-purity nominal plates rather than certified elemental standards.

Because an independent narrow-line FWHM measurement and a retained certified wavelength-calibration spectrum were unavailable, the stated 0.20 nm optical resolution remains nominal. In addition, the 0.25 nm exported sampling interval limits the precision with which peak centres and model-important wavelengths can be localized. Candidate NIST assignments are therefore reported within tolerance windows and as potentially blended spectral regions. The classification results should be interpreted as instrument- and preprocessing-specific internal separability rather than as a resolution-independent spectral-identification model.

Comparison with Previous LIBS Classification Studies. To place the present workflow in the context of previous LIBS classification research, Table 3 compares representative studies involving steels, aluminium alloys, and metallic scrap. The comparison emphasizes the analytical task, classification method, and principal methodological contribution. The purpose is not to claim superior predictive accuracy across different datasets, but to clarify how the present study extends conventional classification by explicitly assessing acquisition-related confounding and separating internal spectral separability from external specimen-level identification.

Table 3. Comparison of representative LIBS classification studies involving metallic materials

Ref.	Materials/application	Analytical method	Principal contribution	Relation to the present study
Liang et al. [22]	Nine types of steel	LIBS–SVM	Comparison of multiclass SVM strategies	Demonstrates established SVM-based steel discrimination
Zhang et al. [23]	Steel samples	Random forest	RF-based classification of LIBS spectra	Provides a direct precedent for RF classification
Campanella et al. [24]	Wrought aluminium alloys from scrap	Artificial neural networks	ANN-based alloy classification	Demonstrates classification of related aluminium-alloy classes
Chen et al. [25]	Steel classes	Deep belief network	Deep-learning classification of steel spectra	Represents a more complex nonlinear modelling approach
Díaz-Romero et al. [26]	Aluminium metal scrap	Deep and conventional machine-learning methods	Real-time metal-scrap classification	Demonstrates application-oriented comparison of ML models
Vors et al. [27]	Alloys	Multivariate classification with robustness evaluation	Emphasis on model robustness	Closely related to the present study's validation-aware motivation
Remus and Dunsin [28]	Multiple LIBS classification tasks	Comparative pattern-classification validation	Emphasis on robust validation	Supports separation of fitted accuracy from robust performance
Present study	Nine nominal metallic classes	Repeatability metrics, PCA, clustering and Random Forest	Acquisition-signature exclusion, metadata-only control, permutation testing and restricted-subset signal-level sensitivity analysis	Explicitly distinguishes internal separability from independent-specimen identification

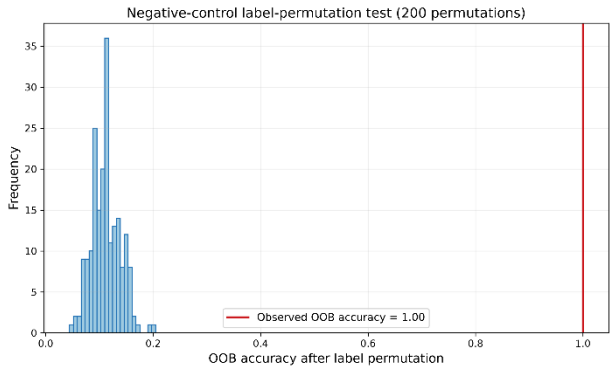

Fig. 6 Negative-control label-permutation test. Randomly permuted labels produced 11.18% ± 2.68 percentage points mean OOB accuracy across 200 runs; the empirical p-value for the observed separation was 0.00498.

CONCLUSION

This exploratory study evaluated a repeatability-aware workflow using 181 moderate-resolution single-shot LIBS spectra from nine nominal metallic material classes. The revised material description explicitly separates nominal elemental specimens from alloy/multicomponent classes and records the verification status of the cobalt, iron, and nickel plates.

Mean within-class correlation ranged from 0.745 to 0.971. PC1 and PC2 explained 63.55% cumulative variance, while the first ten PCs explained 93.33%. Raw mean intensity showed substantial within-class variation and changed its material ordering after restriction to a more uniform acquisition subset, supporting the use of normalized spectral shape for fingerprint comparison while retaining raw amplitude as a separate Repeatability diagnostic.

PCA and hierarchical clustering recovered expected covariance and similarity patterns, including copper–brass and iron–stainless-steel relationships. These relationships are consistent with the revised material classification: brass is a Cu–Zn alloy class and stainless steel is an Fe-based alloy class, whereas cobalt, iron, nickel, aluminium, copper, lead, and titanium are treated as nominal elemental classes. Random forest importance was also physically consistent with candidate Al I, Cu I, Zn I, Pb I, Fe I, and Ti II features, linking the statistical discrimination to plausible atomic-emission regions rather than to arbitrary labels alone.

Independent-specimen validation remains necessary before the workflow can be used for general-purpose identification of unknown metallic materials. Such validation should include multiple independently sourced specimens per class, uniform acquisition settings, and train–test separation performed exclusively at the specimen level. The random forest completely separated the 181 spectra under spectrum-level OOB resampling, but accuracy decreased to 93.37% when complete acquisition signatures were held out. Metadata-only prediction and a significant material–signature association demonstrated acquisition confounding. The label-permutation null distribution was centred at 11.18% accuracy (SD 2.68 percentage points), and none of 200 permutations reached the observed result (empirical $p = 0.00498$; Fig. 6). These results demonstrate non-random internal spectral structure but do not estimate performance on independent specimens.

The acquisition-grouped analysis is now included. The essential

next step is specimen-level validation using multiple independently sourced coupons per class under uniform acquisition settings.

ASSOCIATED CONTENT

The supporting information of this article (Figs. 1–S9 and Table S1) is available at https://www.at-spectrosc.com

AUTHOR INFORMATION

Nugzar Gomidze is a Professor of Physics and Head of the Department of Physics at Batumi Shota Rustaveli State University, Georgia. He received his Candidate of Sciences degree in Physics and Mathematics from Ivane Javakhishvili Tbilisi State University in 1997. He has been a Full Member of the Georgian Academy of Natural Sciences since 2019. His research interests include radiophysics, laser-induced breakdown spectroscopy (LIBS), plasma diagnostics, optical spectroscopy, remote sensing, and environmental monitoring. His recent scientific activities focus on laser-induced plasma processes, spectroscopic characterization of materials, and computational modeling. Professor Gomidze has extensive experience in university teaching, academic administration, international research collaborations, and the supervision of graduate research.

Corresponding Authors

*N. Gomidze

Email address: gomidze@bsu.edu.ge

Notes

The authors declare no competing financial interest.

REFERENCES

1. R. Noll, *Laser-induced breakdown spectroscopy: Fundamentals and applications*, Springer, 2012. https://doi.org/10.1007/978-3-642-20668-9
2. D. A. Cremers, and L. J. Radziemski, *Handbook of laser-induced breakdown spectroscopy*, John Wiley & Sons, 2006. https://doi.org/10.1002/0470093013
3. S. Musazzi, and U. Perini, Eds., *Laser-induced breakdown spectroscopy: Theory and applications*, Springer, 2014. https://doi.org/10.1007/978-3-642-45085-3
4. D. W. Hahn, and N. Omenetto, *Appl. Spectrosc.*, 2010, **64**, 335A–366A. https://doi.org/10.1366/000370210793561691
5. L. J. Radziemski, and D. A. Cremers, Eds., *Laser-induced plasmas and applications*, Marcel Dekker, New York, 1989.
6. H. R. Griem, *Principles of plasma spectroscopy*, Cambridge University Press, 1997. https://doi.org/10.1017/CBO9780511524578
7. N. Konjević, M. Ivković, and S. Jovićević, *Spectrochim. Acta B*, 2010, **65**, 593–602. https://doi.org/10.1016/j.sab.2010.03.009
8. F. F. Chen, *Introduction to plasma physics and controlled fusion*, 3rd ed., Springer, 2016. https://doi.org/10.1007/978-3-319-22309-4
9. H. Hou, Y. Tian, Y. Lu, Y. Li, and R. Zheng, *Appl. Spectrosc.*, 2014, **68**, 1085–1092. https://doi.org/10.1366/13-07350
10. L. Rajačić, N. V. Nedić, D. Dojić, M. Skočić, and S. Bukvić, *J. Quant. Spectrosc. Radiat. Transf.*, 2024, **333**, 109338. https://doi.org/10.1016/j.jqsrt.2024.109338
11. J. A. M. Van der Mullen, *Phys. Rep.*, 1990, **191**, 109–220. https://doi.org/10.1016/0370-1573(90)90152-R
12. Z. Hao, K. Liu, Q. Lian, C. Zhang, X. Li, and R. Zheng, *Front. Phys.*, 2024, **19**, 63301. https://doi.org/10.1007/s11467-024-1427-2
13. Z. Wang, *Chemosensors*, 2025, **13**, 5. https://doi.org/10.3390/chemosensors13010005
14. S. Akbar, M. I. Razzaq, N. Ahmed, et al., *Appl. Spectrosc.*, 2025, **79**, 1129–1141. https://doi.org/10.1177/00037028251334151
15. L. Quackatz, A. Griesche, and T. Kannengiesser, *Spectrochim. Acta B*, 2022, **193**, 106439. https://doi.org/10.1016/j.sab.2022.106439
16. A. Kramida, Yu. Ralchenko, J. Reader, and NIST ASD Team, NIST Atomic Spectra Database (version 5.12), National Institute of Standards and Technology, Gaithersburg, MD, 2024. https://doi.org/10.18434/T4W30F
17. N. Gomidze, D. Jakobia, M. Khajishvili, L. Kalandadze, I. Jabnidze, K. Makharadze, O. Nakashidze, and J. Shainidze, *Ukr. J. Phys.*, 2026, **71**, 173–183. https://ujp.bitp.kiev.ua/index.php/ert/article/view/2023923/3449
18. K. Pearson, *Proc. R. Soc. London*, 1895, **58**, 240–242. https://doi.org/10.1098/rspl.1895.0041
19. C. E. Shannon, *Bell Syst. Tech. J.*, 1948, **27**, 379–423. https://doi.org/10.1002/j.1538-7305.1948.tb01338.x
20. S. Zhao, Y. Zhao, Y. Dai, Z. Liu, and X. Gao, *Spectrochim. Acta B*, 2024, **218**, 106982. https://doi.org/10.1016/j.sab.2024.106982
21. M. Khajishvili, J. Shainidze, K. Makharadze, and N. Gomidze, *Eurasia Proc. Sci. Technol. Eng. Math.*, 2023, **23**, 93–99. https://scispace.com/pdf/on-the-development-of-the-fluorescence-excitation-emission-287da3h7s7.pdf
22. L. Liang, T. Zhang, K. Wang, H. Tang, X. Yang, X. Zhu, Y. Duan, and H. Li, *Appl. Opt.*, 2014, **53**, 544–552. https://doi.org/10.1364/AO.53.000544
23. T. Zhang, D. Xia, H. Tang, X. Yang, and H. Li, *Chemom. Intell. Lab. Syst.*, 2016, **157**, 196–201. https://doi.org/10.1016/j.chemolab.2016.07.001
24. B. Campanella, E. Grifoni, S. Legnaioli, G. Lorenzetti, S. Pagnotta, F. Sorrentino, and V. Palleschi, *Spectrochim. Acta B*, 2017, **134**, 52–57. https://doi.org/10.1016/j.sab.2017.06.003
25. G. Chen, Q. Zeng, W. Li, X. Chen, M. Yuan, L. Liu, H. Ma, B. Wang, Y. Liu, L. Guo, and H. Yu, *Opt. Express*, 2022, **30**, 9428–9440. https://doi.org/10.1364/OE.451969
26. D. J. Díaz-Romero, S. Van den Eynde, W. Sterkens, A. Eckert, I. Zaplana, T. Goedemé, and J. Peeters, *Spectrochim. Acta B*, 2022, **196**, 106519. https://doi.org/10.1016/j.sab.2022.106519
27. E. Vors, K. Tchepidjian, and J.-B. Sirven, *Spectrochim. Acta B*, 2016, **117**, 16–22. https://doi.org/10.1016/j.sab.2015.12.004
28. J. Remus, and K. S. Dunsin, *Appl. Opt.*, 2012, **51**, B49–B56. https://doi.org/10.1364/AO.51.000B49
29. J. M. Mermet, P. Mauchien, and J. L. Lacour, *Spectrochim. Acta B*, 2008, **63**, 999–1005. https://doi.org/10.1016/j.sab.2008.06.003
30. F. Chang, J. Yang, H. Lu, and H. Li, *J. Anal. At. Spectrom.*, 2021, **36**, 1712–1723. https://doi.org/10.1039/D1JA00040C